remote sensing

MDPI

Article

DEM Generation with ICESat-2 Altimetry Data for the Three Antarctic Ice Shelves: Ross, Filchner–Ronne and Amery

Tong Geng, Shengkai Zhang *, Feng Xiao, Jiaxing Li, Yue Xuan, Xiao Li and Fei Li

Chinese Antarctic Center of Surveying and Mapping, Wuhan University, Wuhan 430079, China; t.geng@whu.edu.cn (T.G.); shaw89@whu.edu.cn (F.X.); listening@whu.edu.cn (J.L.); xuanyue@whu.edu.cn (Y.X.); lx850569127@whu.edu.cn (X.L.); fli@whu.edu.cn (F.L.)

* Correspondence: zskai@whu.edu.cn

Abstract: The ice shelf is an important component of the Antarctic system, and the interaction between the ice sheet and the ocean often proceeds through mass variations of the ice shelf. The digital elevation model (DEM) of the ice shelf is particularly important for ice shelf elevation change and mass balance estimation. With the development of satellite altimetry technology, it became an important data source for DEM research of Antarctica. The National Aeronautics and Space Administration (NASA) Ice, Cloud, and Land Elevation Satellite-2 (ICESat-2) launched in 2018 is a significant improvement in along-track sampling rate and measurement accuracy compared with previous altimetry satellites. This study uses ordinary kriging interpolation to present new DEMs (ICESat-2 DEM hereinafter) for the three ice shelves (Ross, Filchner–Ronne and Amery) in Antarctica with ICESat-2 altimetry data. Two variogram models (linear and spherical) of ordinary kriging interpolation are compared in this paper. The result shows that the spherical model generally shows better performance and lower standard deviation (STD) than the linear models. The precision of the ultimate DEM was evaluated by NASA Operation IceBridge (OIB) data and compared with five previously published Antarctic DEM products (REMA, TanDEM-X PolarDEM, Slater DEM, Helm DEM, and Bamber DEM). The comparison reveals that the mean difference between ICESat-2 DEM of the Ross ice shelf and OIB is −0.016 m with a STD of 0.918 m, and the mean difference between ICESat-2 DEM of the Filchner–Ronne ice shelf and OIB is −0.533 m with a STD of 0.718 m. The three ICESat-2 DEMs show higher spatial resolution and elevation accuracy than five previously published Antarctic DEMs.

Keywords: digital elevation model; Antarctic ice shelf; ICESat-2; kriging; satellite altimeter

check for updates

Citation: Geng, T.; Zhang, S.; Xiao, F.; Li, J.; Xuan, Y.; Li, X.; Li, F. DEM Generation with ICESat-2 Altimetry Data for the Three Antarctic Ice Shelves: Ross, Filchner–Ronne and Amery. *Remote Sens.* **2021**, *13*, 5137. https://doi.org/10.3390/rs13245137

Academic Editor: Alexander Braun

Received: 5 November 2021
Accepted: 16 December 2021
Published: 17 December 2021

Publisher's Note: MDPI stays neutral with regard to jurisdictional claims in published maps and institutional affiliations.

Copyright: © 2021 by the authors. Licensee MDPI, Basel, Switzerland. This article is an open access article distributed under the terms and conditions of the Creative Commons Attribution (CC BY) license (https://creativecommons.org/licenses/by/4.0/).

1. Introduction

The ice shelf is the part of land ice that extends over the ocean and floats on it. There are many major or minor ice shelves surrounding the Antarctic coastline, and glaciers on the ice sheet drain into the ocean across the ice shelves. They cover more than 1.561 million km^2 [1], accounting for three quarters of Antarctica's coastline [2]. Ice shelf mass balance has a significant impact on global climate change, ecological change, and human social development. Iceberg calving from the ice shelf is a major process of Antarctic mass loss, and it has been regarded as a crucial variable in precisely evaluating the mass balance of ice shelves. In addition, ice shelf basal melt is also a key factor affecting the mass balance of Antarctica [3–5]. The flow of outlet glacier ice is buttressed or restrained by the ice shelf. Therefore, ice shelf collapse will lead to accelerated glacier flow and retreating coastlines [6–8].

As one of the most basic geographic data, ice shelf surface elevation datasets provide information critical for glaciological studies. The digital elevation model (DEM) of the Antarctic ice shelf is particularly important for planning of fieldwork, numerical flow modeling, and ice movement tracking [9–11]. Accurate knowledge of the ice

sheet and ice shelf elevation can be used for the determination of subglacial hydrological pathways [12–14]. By combining the DEM with other datasets, ice thickness at the edge of the ice shelf and drainage basin areas can be measured and then the mass balance of the ice shelf can be estimated using a mass budget approach [15–17].

DEMs for different periods are also indispensable for calculating elevation and mass changes to support ice dynamics studies and sea level change estimates [18–20]. Furthermore, detailed and spatially and temporally matched DEMs are required for calibration to obtain accurate geographical information on the ice sheet or ice shelf when using remote sensing data for polar research. [21,22].

Broad-scale fieldwork is difficult to plan in the Antarctica due to the remote geolocation and extreme environment. Therefore, most of the previously published Antarctic DEMs were derived based on satellite remote-sensing data. DEMs [23–26] were derived from radar altimeters data such as ERS-1/2 and CryoSat-2, which are unaffected by clouds and can, therefore, enable continuous observations but have low elevation accuracy, especially in highly inclined areas. The ICESat DEM [27] derived from ICESat/GLAS, which is the first laser altimeter used for the cryosphere, is limited in ice sheet margins due to its coarse across-track resolution. The DEM [9] based on the combination of ICESat and ERS-1 elevation measurements improves the coverage but has limited accuracy and spatial resolution. In addition, released 90 m TanDEM-X PolarDEM [28] is based on the Interferometric Synthetic Aperture Radar (InSAR) with large errors inside the ice sheet and X-band radar signals penetrate up to several meters into the firn covering the ice sheet and ice shelf [29–32], and errors increase with surface slope [33,34]. The Reference Elevation Model of Antarctica (REMA) [35] was created from stereo-photogrammetry using DigitalGlobe satellite imagery with high spatial resolution but small gaps affected by clouds, hill shade, and time registration [36], mainly in areas of complex topography and continuous cloud cover such as the Antarctic Peninsula.

As a follow-on satellite to the first generation of ICESat mission, the ICESat-2 satellite has been in an orbit with repeat cycle of 91 days since September 2018. The satellite altimetry data provided by ICESat-2 allows the detection of land ice height and sea ice thickness changes, and the acquisition of global land vegetation height. The Advanced Topographic Laser Altimeter System (ATLAS) for ICESat-2 is a single photon measurement sensor using only the green light laser band [37]. ICESat-2/ATLAS operates with six separate beams, which are deployed in three-beam pairs, and each of them one contains both strong and weak signals, and the two signals differ in energy by four times. The spacing between each two pair of tracks is 3 km, and the spacing between strong and weak beams is only 90 m. Compared to the ICESat satellite, ICESat-2 reduces the laser footprint to 17 m and the sampling distance along the orbital direction to only 0.7 m. Multi-beam pairs can provide more observations and greatly improve spatial resolution compared with ICESat/GLAS [38]. Effective use of small track spacing also allows calculation of cross-track slopes to improve elevation accuracy in Antarctic margins and steep regions [39].

The interpolation method becomes an important factor affecting the accuracy of the DEM when a high-quality and dense surface elevation data from satellite measurements acquired. Previous studies have shown that kriging interpolation based on geostatistics is considered to be an effective spatial interpolation method and is widely used in studies of ice sheet surface elevation changes and mass balance [40–44]. Variogram models will affect the interpolation results in the generation of DEM by the kriging interpolation method [45].

Two representative variogram models (linear and spherical) of ordinary kriging are calculated and compared in this study. We then used the one-year sequence of elevations acquired by ICESat-2 between October 2019 and October 2020 to obtain 100 m spatial resolution DEM for the Ross, Filchner–Ronne, and Amery ice shelves. In addition, we verified the accuracy of the established DEM using the available NASA Operation IceBridge (OIB) airborne laser altimetry data. The performances are also compared with other published Antarctic DEMs covering the three ice shelves of Antarctica.

2. Study Areas

The Ross ice shelf (RIS), Filchner–Ronne ice shelf (FRIS), and Amery ice shelf (AIS) are the three most dominant ice shelves in Antarctica (Figure 1).

RIS is located in the west Antarctica, with a latitude of 77°23′S to 85°13′S and a longitude of 147°4′W to 158°10′W, adjacent to the Ross Sea, between the King Edward VII Peninsula and Ross Island, with the Queen Maud Mountains to the south and Marie Bird Land to the east, and the largest island within the RIS is Roosevelt Island. As the largest ice shelf in Antarctica, RIS covers an area of approximately 470,000 km^2 [46].

FRIS is located along the coast of the Weddell Sea in west Antarctica, with a latitude of 72°24′S to 83°29′S and a longitude of 22°33′W to 8°53′W, covering approximately 430,000 km^2, bordered by the Weddell Sea to the north, the Ellsworth Mountains to the south and the Antarctic Peninsula and the Edith Ronne Land are on the east and west sides of the ice shelf. The ocean-facing side of the FRIS is split into an eastern (Filchner) and a western (Ronne) part by Berkner Island [47].

AIS is supplied by the Lambert Glacier, located near the Prydz Bay between Larsemann Hills and Prince Charles Mountains, with a latitude of 68°29′S to 73°19′S and a longitude of 66°20′E to 74°23′W. With an area of about 60,000 km^2, this ice shelf is the third largest in Antarctica, after the RIS and FRIS [48].

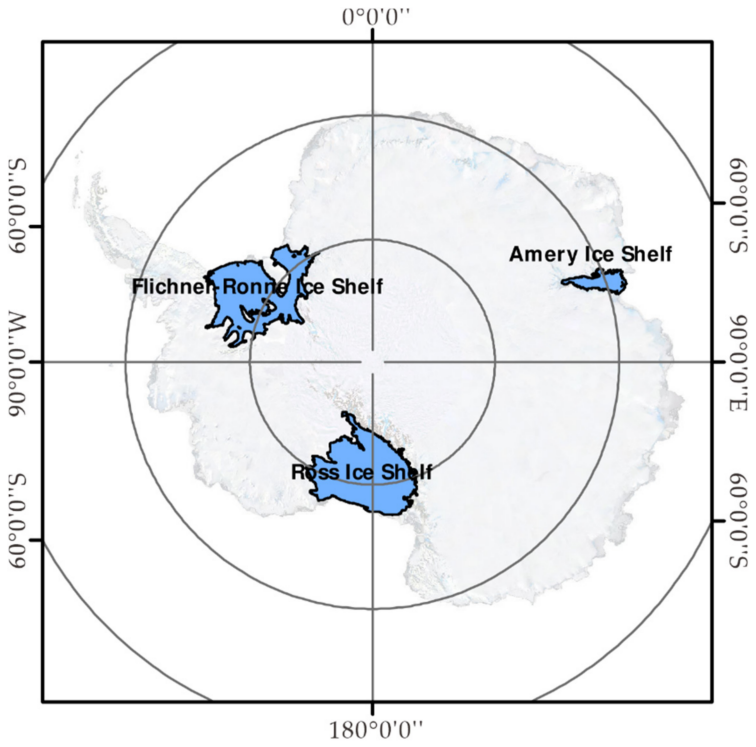


Figure 1. Locations of Ross ice shelf (RIS), Filchner–Ronne ice shelf (FRIS), and Amery ice shelf (AIS). The backgrounding map is the Landsat Image Mosaic of Antarctica (LIMA) [49].

3. Data

3.1. Ice, Cloud, and Land Elevation Satellite-2 (ICESat-2) Data

The ICESat-2 ATL06 land ice elevation product from October 2019 to October 2020 is used in this study, with a total of 370,019,727 sampling points. On the basis of the ATL03 photon dataset, ATL06 is developed by the along-track photon data divided from each beam into short (40 m) overlapping segments [50].

In the ATL06 product, biased surface elevations due to truncation of the return pulse are greatly reduced (correction to decrease the magnitude of deviation to less than 1 mm) by correction of transmit pulse shape bias; the accuracy is improved by correction of first-

photon bias due to detector delay in areas with higher roughness and weaker reflection [51]. Abdalati and others (2010) pre-tested the performance of ICESat-2 and the results showed that under complex terrain conditions, there is mean deviation of less than 14 cm with root mean squared error values between 22 and 46 cm compared by OIB data [38] Brunt and others (2019) validated the ATL06 product using GNSS data, and the results showed that the elevation bias of ATL06 is less than 3 cm [52]; Li and others (2021) obtained the ATL06 datasets elevation accuracy of 1.5 cm compared by coordinated multi-sensor observations [53]. Adequate validation results indicate that ICESat-2 high accuracy satellite measurement data are the guarantee of an accurate DEM generation.

3.2. Operation IceBridge (OIB) Airborne Topographic Mapper (ATM)

The Airborne Topographic Mapper (ATM) belonging to the U.S. NASA's OIB is a conically scanning laser altimeter that combines the use of a global positioning system (GPS) for positioning with an inertial navigation system (INS) for orientation measurement and works at a wavelength of 532 nm and a swath width of 140 m with a nominal footprint size of 1 m. ATM data using WGS-84 as the reference ellipsoid and ITRF-2005 as the reference frame and vertical elevation accuracy of it is 0.1 m with a horizontal coordinate accuracy of 1 m for flat ice sheets [54,55]. The OIB ATM L2 ice elevation, slope, and roughness (V002) product [56] is used in this study, which is resampled and averaged from ATM L1B data. Considering the lack of missions on the AIS, we only provide an independent validation of the RIS and FRIS DEMs and apply OIB airborne data in October 2013 and October 2016.

3.3. Previously Published Antarctic Digital Elevation Models (DEMs)

Five previously published Antarctic DEM products, namely, Bamber DEM [9], Helm DEM [24], Slater DEM [26], REMA [35], and TanDEM-X PolarDEM, are compared with the ICESat-2 DEM [28]. General information concerning these DEMs is provided in Table 1.

Table 1. General information of five previously published Antarctic digital elevation models (DEMs).

	Bamber DEM	**Helm DEM**	**TanDEM-X PolarDEM**	**Slater DEM**	**REMA**
Published time	2009	2014	2017	2018	2018
Source data	ERS-1 and ICESat	CryoSat-2	TerraSAR-X and TanDEM-X	CryoSat-2	WorldView-1/2/3 and GeoEye-1
Coverage	Ice sheet	Pan-Antarctica	Global	Pan-Antarctica	Pan-Antarctica
Spatial resolution	1 km	1 km	12 m, 30 m, 90 m	1 km	8 m, 100 m, 200 m, 1 km
Time span of applied source data	March 1994–May 1995, February 2003–March 2008	January 2012–January 2013	December 2010–January 2015	July 2010–July 2016	2010–2018

3.3.1. Bamber DEM

Bamber and others (2009) generated a DEM (called Bamber DEM) of Antarctica at resolutions of 1 km by combining satellite altimetry data from two different sources, laser altimeter measurements from ICESat mission (variable between 200 and 2007) and SRA data from the ERS-1 satellite mission (collected in March 1994). The former provides decimeter vertical accuracy, and the latter has excellent spatial coverage. Bamber DEM fully combines the high accuracy of ICESat measurement data with ERS-1 high spatial resolution in the edge region of Antarctica by interpolation of elevation estimation. The elevation accuracy and spatial resolution of the DEM are optimized, and the number of cells in the grid is minimized. However, the spatial resolution of published Bamber DEM varies from 1 km to 5 km, and the DEM resolution is 5 km in areas with only radar altimetry data; the DEM The resolution reaches 1 km in the area with dense laser altimetry data.

3.3.2. Helm DEM

On the basis of 3 years of CryoSat-2 data acquisition, Helm and others (2014) derived a DEM (called Helm DEM) of Antarctica covering ice sheet south of 60° S, which is referenced to WGS84. Before DEM establishment, the waveform data were retrieved using a modified threshold first maximum re-tracker method, and then the low-resolution mode (LRM) and SARIn data were slope corrected using the relocation operation and the phase difference approach respectively. The ordinary kriging interpolation is used in DEM generation and the final spatial resolution of Helm DEM is limited to 1 km.

3.3.3. TanDEM-X PolarDEM

The TanDEM-X mission is to acquire a high-resolution global DEM that includes the Antarctic ice sheet. It consists of a double star system, including TerraSAR-X (launched in 2007) and TanDEM-X (launched in 2010). The TerraSAR-X and TanDEM-X equipped with SAR at X-band can provide the observation data required by the global terrestrial high-precision digital elevation model. TanDEM-X Global DEM is derived from SAR data in StripMap mode using horizontal transmit polarization and receive polarization from December 2010 to January 2015 [28]. The TanDEM-X PolarDEM is referenced to WGS-84 ellipsoid and has three resolution versions of 12, 30, and 90 m. The TanDEM-X PolarDEM at resolutions of 90 m is used for comparison in this study to reduce error from resampling.

3.3.4. Slater DEM

Slater and others (2018) presented a DEM (called Slater DEM) of the Antarctic with the resolution of 1 km and the radar altimeter data used was acquired fromCryoSat-2 satellite mission between July 2010 and July 2016. The offset centre of gravity (OCOG) re-tracking algorithm was applied to re-track the altimeter waveform. Within each Slater DEM grid, the same quadratic function is used and the function is solved by least squares to obtain the representative elevation values of the grid. The DEM takes into account the effects of backscatter and elevation changes and eventually covers most of the Antarctic region, with only the grid cells north of 88° S obtained by kriging interpolation.

3.3.5. Reference Elevation Model of Antarctica (REMA)

REMA was derived from high-resolution optical images acquired by commercial remote-sensing imaging satellites: the satellite series of WorldView (WorldView-1, WorldView-2, WorldView-3) and GeoEye-1. The automated stereo-photogrammetric technology was applied and the DEMs are registered to CryoSat-2 data and ICESat data. However, some DEM strips are missed due to rejection by quality control or missing registration. Gaps in the low-resolution version (except for 8 m resolution) of the REMA are filled with previously published DEMs (ASTER GDEM [57] at 100 m resolution and Helm DEM at 1 km resolution). Four resolution versions of REMA with spatial resolution of 8 m, 100 m, 200 m, and 1 km are available. We choose the REMA at resolutions of 100 m for comparison to reduce the bias from the resample process.

4. Methods

4.1. Geostatistical Modeling

The kriging method, which is also known as estimation of local spatial scale, is a commonly used spatial interpolation method in geographical information systems [58]. The variogram describes the spatial continuity of the data and is the central tool of geostatistics. It enables scientists to assess whether their data are spatially correlated and to what extent [59]. Variation analysis of the kriging method is modeled in a space composed of sampling points. A semivariogram that represents the relationship between the semivariance $\varphi(l)$, and the lag distance h is defined by:

$$\varphi(h) = \frac{1}{2}E[H(x) - H(x+l)]^2 \quad (1)$$

where $H(x)$ is the measured elevation sample value of ICESat-2, and $H(x+l)$ is the measured sample value at another point displaced from the point x by a lag distance h.

There are three elements of the variogram model. The sill is the upper limit of the model, which is the a priori variance of a second-order smooth stochastic process [58]. At a finite lag distance, a variogram may reach its sill and the correlation range represents this range. In other words, the data have no spatial correlation beyond this range. The nugget variance means measurement error and its numerical value is the value of variogram when lag distance is zero. Through the variogram model, Kriging maximizes the use of available information by considering the way attributes vary in space. The spherical and linear models are the two most commonly used models in earth sciences, and they are computed and compared in this paper. These models are defined by the following equations:

Spherical model:

$$\varphi(l) = \begin{cases} 0 & l = 0 \\ c_0 + c \times \frac{3}{2} \times \frac{l}{a} - \frac{1}{2} & a \geq l > 0 \\ c + c_0 & l > a \end{cases} \quad (2)$$

Linear model:

$$\varphi(h) = \begin{cases} 0 & l = 0 \\ c_0 + c\left(\frac{l}{a}\right) & a \geq l > 0 \\ c + c_0 & l > a \end{cases} \quad (3)$$

To determine which model is the optimal, an experimental area is selected from the RIS, the FRIS, and the AIS. Then, linear variogram model and spherical variogram model are used to generate DEM of experimental areas independently. Final DEMs are shown in Figure 2.

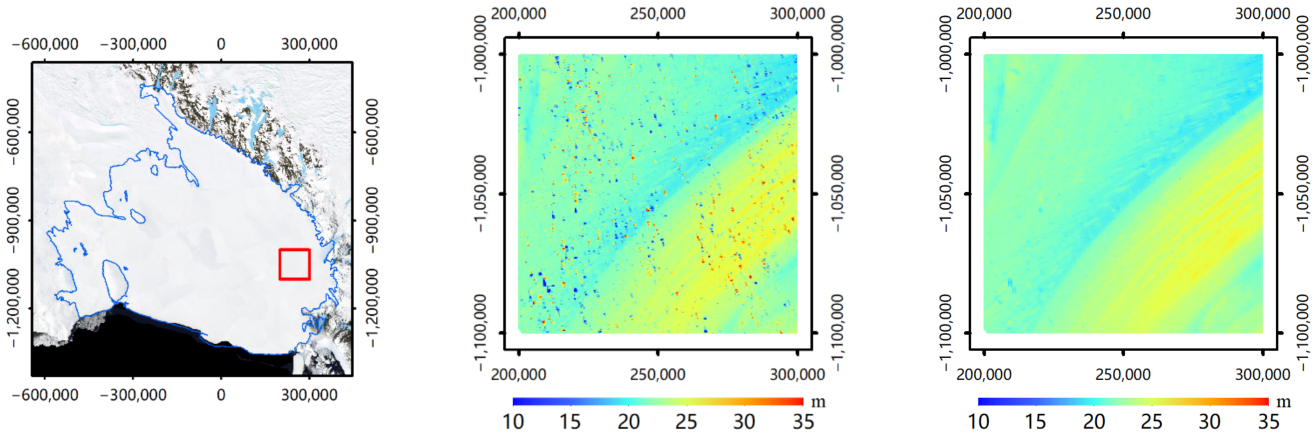


Figure 2. *Cont.*

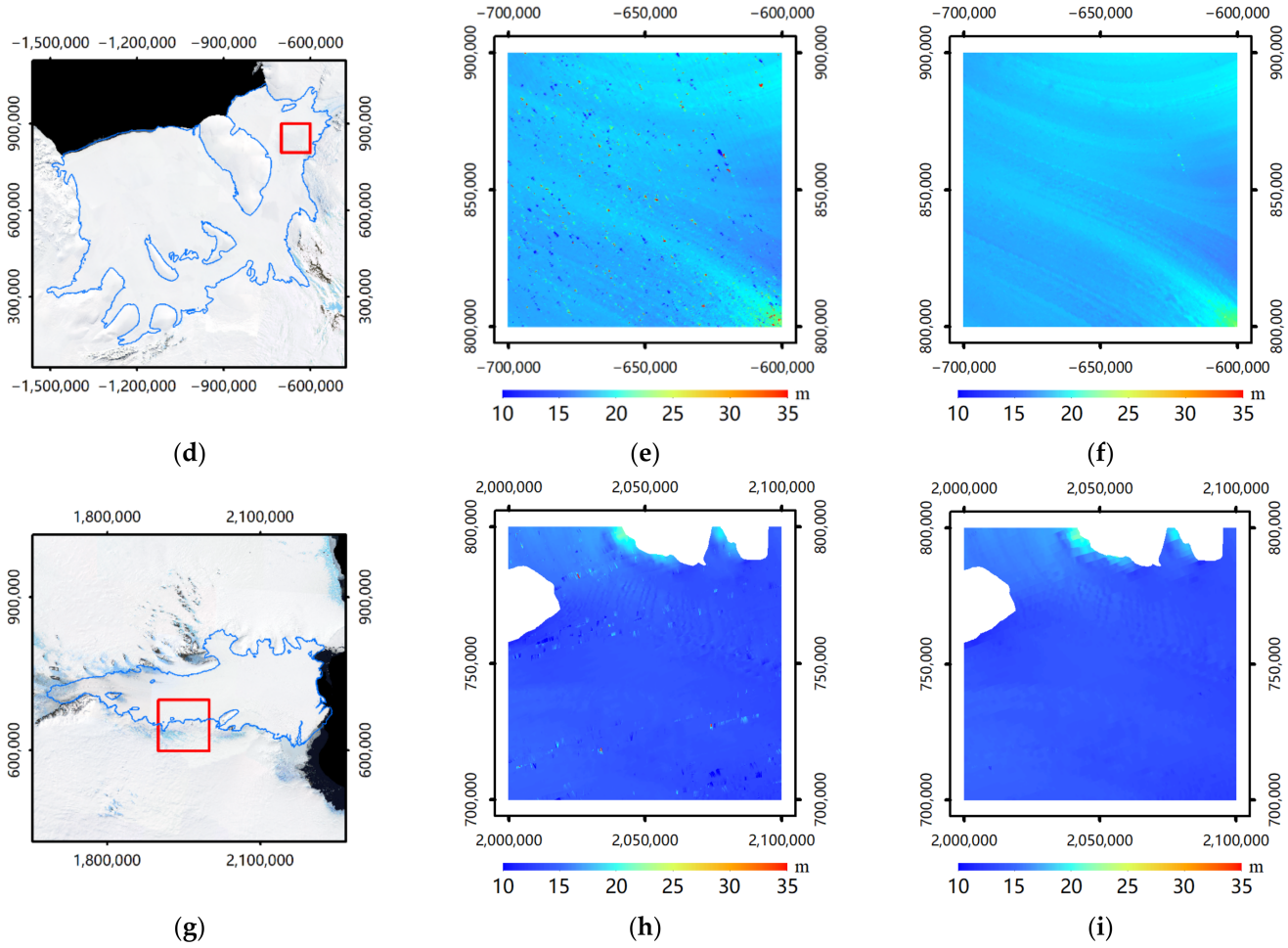


Figure 2. Digital elevation models (DEMs) of experimental areas in the RIS, the FRIS, and the AIS derived from Ice, Cloud, and Land Elevation Satellite-2 (ICESat-2) data by kriging with linear variogram model and spherical variogram model. (**a**) experimental areas in the RIS; (**b**) RIS DEM based on linear variogram model; (**c**) RIS DEM based on spherical variogram model; (**d**) experimental areas in the FRIS; (**e**) FRIS DEM based on linear variogram model; (**f**) FRIS DEM based on spherical variogram model; (**g**) experimental areas in the AIS; (**h**) AIS DEM based on linear variogram model; (**i**) AIS DEM based on spherical variogram model. The areas in the red box are the experimental areas and the blue line is the coastline. Maps are in the polar stereographic projection in meters.

To cross-validate these kriging models, we divide the ICESat-2 data into a training and validation datasets. For each experimental area, we randomly select 1% ICESat-2 data as a validation dataset. The results of cross validation listed in Table 2 show that the spherical variogram model generally shows lower standard difference than the linear variogram models, but the difference of mean differences is negligible. In particular, linear variogram will generate height anomaly at DEM shown in Figure 2b,e,h.

Table 2. Cross validation result for RIS, FRIS, and AIS DEMs.

	RIS		FRIS		AIS	
Variogram Model	**Linear**	**Spherical**	**Linear**	**Spherical**	**Linear**	**Spherical**
Mean/m	0.011	0.032	−0.016	0.018	−0.006	−0.004
Std/m	2.979	2.769	3.376	2.215	2.287	1.394

4.2. DEM Processing

RIS, FRIS, and AIS DEMs at resolutions of 100 m using the ordinary kriging method based on ICESat-2 measurement points from October 2019 and October 2020 are generated by processing as Figure 3.

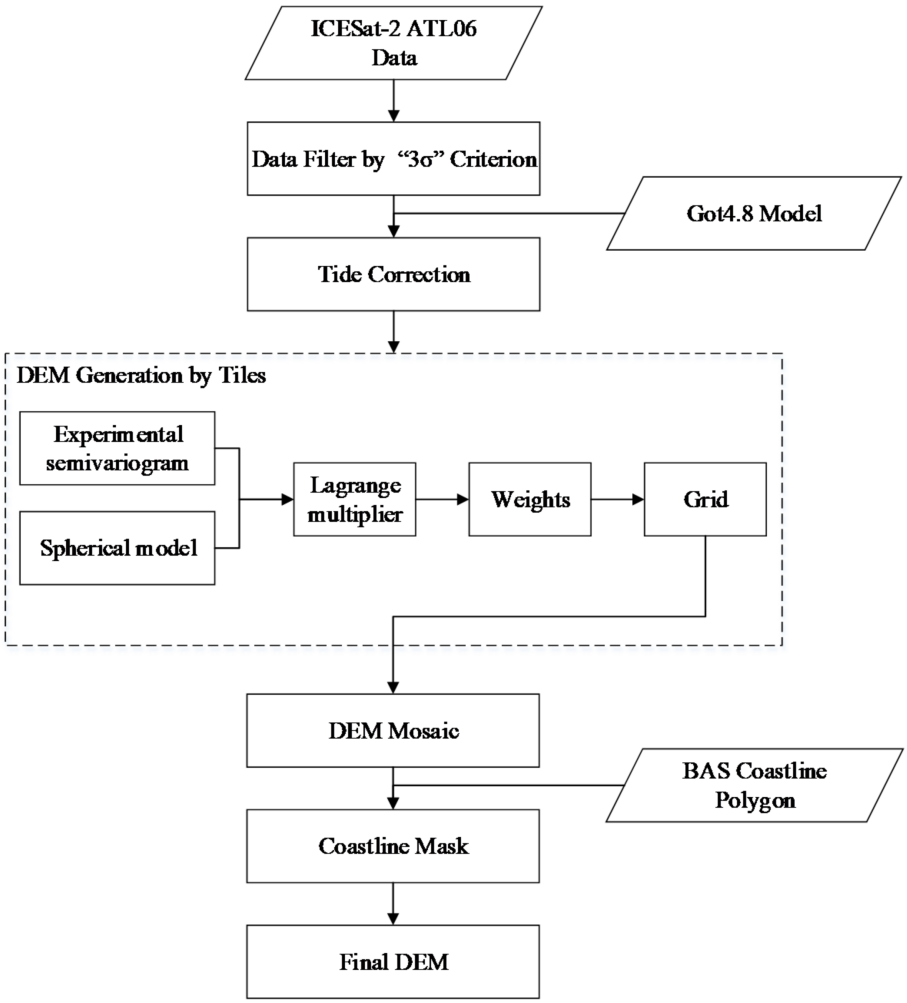


Figure 3. Flow diagram of final DEM generation.

4.2.1. Data Pre-Processing

Although only data marked as good quality (atl06_quality_summary = 0) are used for DEM generation, some obvious error points are still visible, which may be due to residual clouds or other product generation processes that affect the height estimation. Second, the statistical criterion "3σ" is applied on ICESat-2 data, which calculates the mean and standard deviation of ICESat-2 points within each 100 m grid, and remove points that deviate from the elevation mean by more than three times the standard deviation [60]. Eventually, 30,012 abnormal points are discarded, which is approximately 0.01% of the total points sampled.

4.2.2. Tide Correction

An ice shelf is floating on the ocean will be subject to the ocean tides, which results in fluctuations in ice shelf surface elevation. Therefore, ocean tide correction is necessary. However, by default, ICESat-2 ATL06 data are corrected for all height increments in the geophysical parameter's group except for the ocean tide. Here, the GOT4.8 model [61] is applied in this study, which is recommended by Algorithm Theoretical Basis Document for Global Geolocated Photons ATL03 Release 004 [62].

4.2.3. DEM Generation by Tiles

To reduce the processing time, ICESat-2 data are assigned into tiles with resolution of 100 km (Figure 4). To obtain an elevation-continuous DEM, a 10 km-wide buffer zone is placed between each tile. The Ordinary Kriging method is applied to every tile. Firstly, an experimental semivariogram based on satellite altimetry data within the tiles is modeled. Then, the experimental semivariogram which is a discrete function model is fitted using the best fit model for measurements in ice shelves: spherical function model (related experiments showed in Section 4.1). Furthermore, the Lagrange multiplier method can be used to calculate the weights of each sampling point location in the domain that minimizes the kriging variances, and the sum of the weights is restricted to be equal to 1. Finally, in order to estimate the elevation of the center point of each grid, a weighted moving average method is applied, which has parameters such as search radius (1 km and 10 km), search direction (8 directions), maximum (64 points) and minimum (8 points) number of search points.

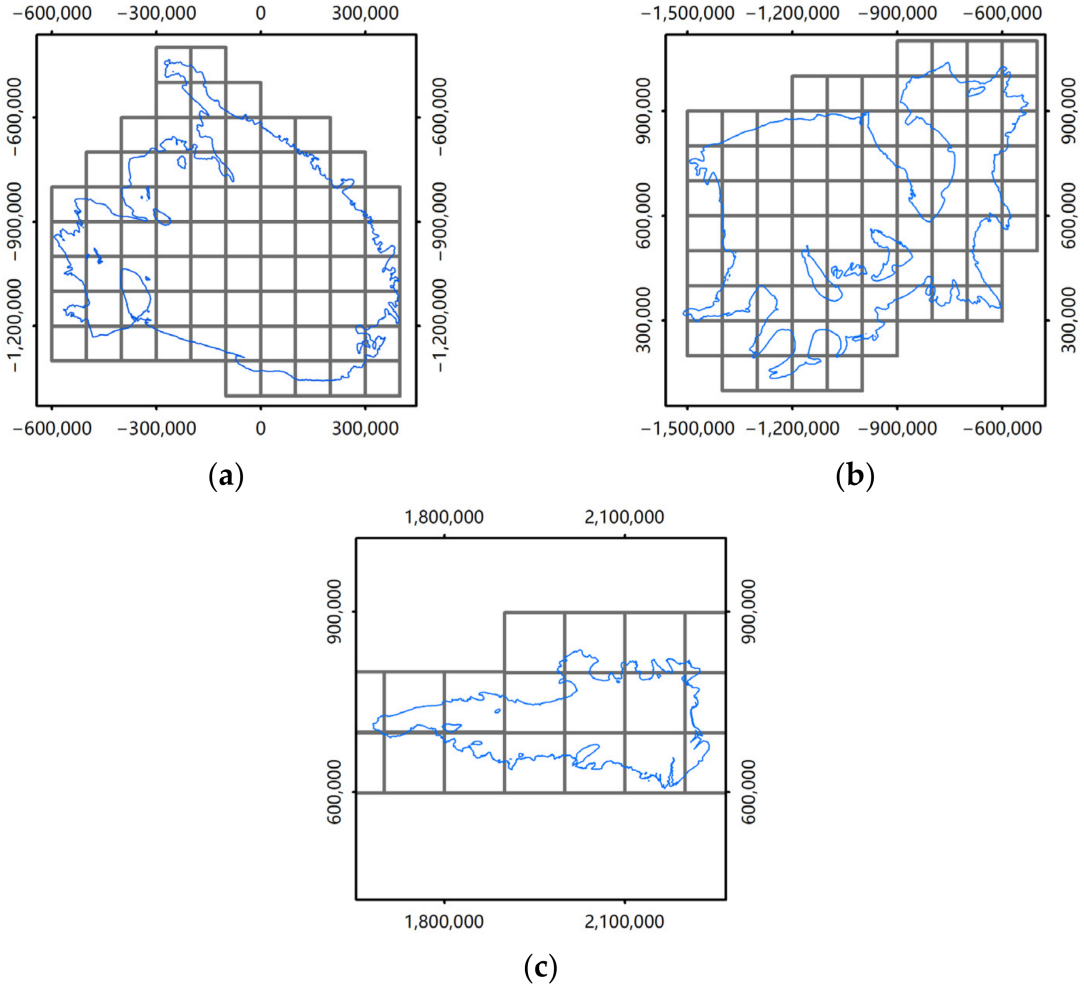


Figure 4. The 100 km by 100 km tiles of RIS, FRIS, and AIS DEMs. Maps are in the polar stereographic projection in meters. The small grey box in the diagram (**a**–**c**) represents the tile of division.

There are two different grids derived from different search radii. The first grid has a spatial resolution of 100 m with a search radius of 1 km; the second grid has a spatial resolution of 1 km with a search radius of 10 km. In order to ensure the reliability of elevation values within each grid, only retain valid grids where more than eight data points are found in one of the available eight sectors of the search circle. This will create some gaps in the 100 m resolution and these gaps will be filled by low-resolution grids. This

method prevents one-way weighting along the orbit and guarantees uniform weighting, since the data coverage is very high along the orbit, but may be sparse across the orbit [24].

4.2.4. DEM Mosaic

Bilinear interpolation is used in tile mosaic processing to fill gaps due to data missing, which is an expansion of the functional linear interpolation, used to interpolate two variables (e.g., x and y) in a linear two-dimensional grid [35]. For overlap between neighboring tiles, a distance-weighted method is applied for processing of DEM data at the boundary, while the weighting factors are gained from distance to strip boundaries.

4.2.5. Coastline Mask

The Antarctic coastline dataset acquired from British Antarctic Survey (BAS) [63] is applied for coastline mask, which is generated from multiple topographic data. However, this coastline with a low resolution does not accurately match the ICESat-2 DEM in some areas. Therefore, the coastline is corrected by a visual interpretation method using ArcGIS software.

5. Result

New ICESat-2 DEMs provide elevation value for RIS, FRIS, and AIS, mapped in Figure 5 in the polar stereographic projection (central meridian of 0° and standard latitude of −71° S) in meters, and referenced to the WGS84 ellipsoid. The terrain of all three ice shelves is relatively flat, and the elevations gradually decrease from inland to the coastal edge of the ice shelf. Elevation statistics of three ice shelves in Table 3 shows that AIS with a mean elevation of 97.192 m and a standard deviation of 38.412 m; RIS with a mean elevation of 9.772 m and the standard deviations of 24.087 m; FRIS with a mean elevation of 73.213 m and a standard deviation of 31.082 m. In addition, the maximum elevation values for RIS, FRIS, and AIS are 1280.716, 925.373, and 1176.542 m, respectively. Meanwhile, the minimum values are −5.441, −21.361, and −15.466 m. Although we use coastline product and operated a coastline correction, a few mountain and oceanic grids along the edge of the ice shelf are included. This condition leads to an anomaly of the elevation maximum and minimum values, and resulted in a high overall standard deviation. Currently, the measurement of ice shelf edge areas and complex terrain is still a challenging problem for satellite altimetry data.

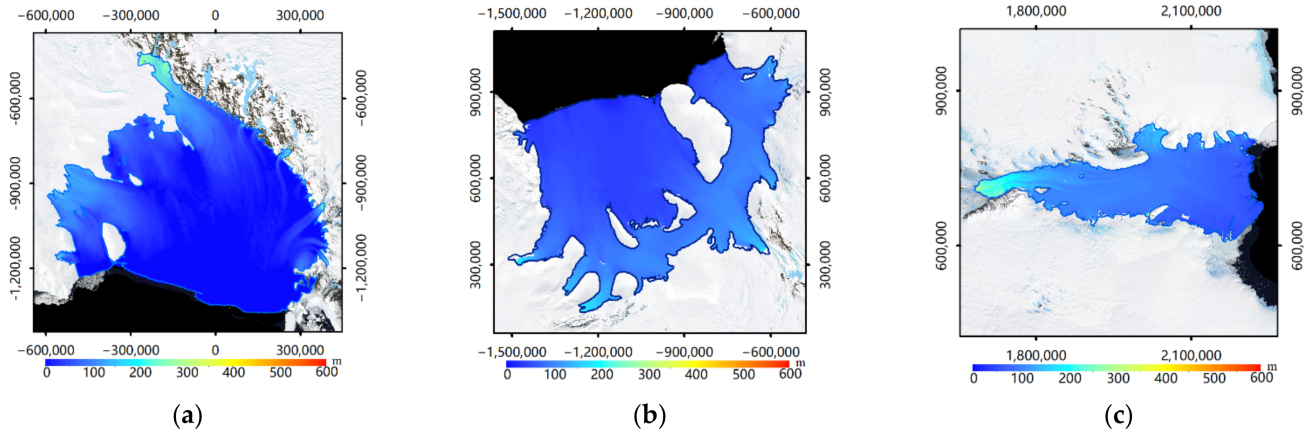


Figure 5. RIS DEM (**a**), FRIS DEM (**b**), and AIS DEM (**c**) at a resolution of 100 m derived from ICESat-2. The black area is the ocean; the blue line is the corrected coastline. Maps are in the polar stereographic projection in meters.

Table 3. Elevation statistics of RIS, FRIS, and AIS DEMs.

	Mean/m	Std/m	Maximum/m	Minimum/m
RIS DEM	9.772	24.087	1280.716	−5.441
FRIS DEM	73.213	31.082	925.373	−21.361
AIS DEM	97.192	38.412	1176.542	−15.466

6. Discussion

6.1. Comparisons with Previous Published DEMs

ICESat-2 RIS, FRIS, and AIS DEMs are compared with five publicly available Antarctic DEMs (REMA, TanDEM-X PolarDEM, Slater DEM, Helm DEM, and Bamber DEM). DEMs with different spatial resolutions are united by resampling a high-resolution DEM to a low-resolution DEM based on bilinear interpolation. The results of absolute elevation difference less than 20 m are shown in Tables 4–6.

As shown in Table 4 and Figure 6, the mean elevation differences between the ICESat-2 RIS DEM and REMA, Slater DEM, Helm DEM, and Bamber DEM are all within 1 m and the standard deviations are within 3 m. The mean elevation difference with TanDEM-X PolarDEM is 4.940 m with a standard deviation of 2.767 m. The elevation difference distribution map (Figure 6) shows that the large elevation differences on the RIS are mainly distributed at the ice shelf edge and the ice cracks inside the ice shelf, which is due to poor accuracy of satellite altimetry in the ice shelf edge region.

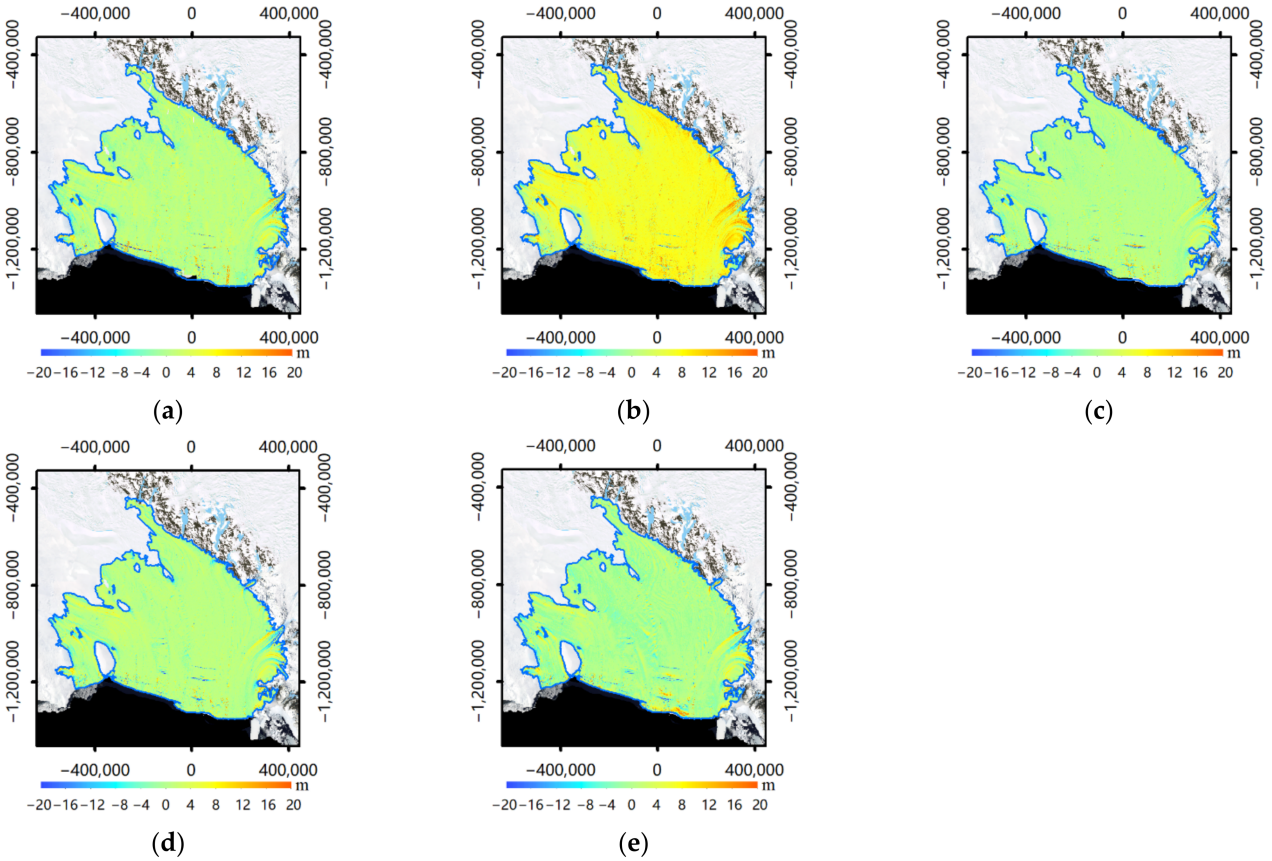


Figure 6. Distribution of elevation differences between the ICESat-2 RIS DEM and five previously published Antarctic DEMs, i.e., Reference Elevation Model of Antarctica (REMA) (**a**), TanDEM PolarDEM (**b**), Slater CryoSat-2 DEM (**c**), Helm CryoSat-2 DEM (**d**), Bamber DEM (**e**). Maps are in the polar stereographic projection in meters.

Table 4. Comparisons between the ICESat-2 RIS DEM and five previously published Antarctic DEMs.

ICESat-2 RIS DEM vs.	Mean/m	Std/m
REMA	0.715	2.493
TanDEM-X PolarDEM	4.940	2.767
Slater DEM	0.408	2.290
Helm DEM	0.536	2.824
Bamber DEM	−0.022	2.674

Table 5. Comparisons between the ICESat-2 FRIS DEM and five previously published Antarctic DEMs.

ICESat-2 FRIS DEM vs.	Mean/m	Std/m
REMA	−0.228	2.955
TanDEM-X PolarDEM	1.738	3.476
Slater DEM	0.674	2.640
Helm DEM	0.956	4.604
Bamber DEM	0.510	3.012

Table 6. Comparisons between the ICESat-2 AIS DEM with five previously published Antarctic DEMs.

ICESat-2 AIS DEM vs.	Mean/m	Std/m
REMA	−0.116	5.294
TanDEM-X PolarDEM	1.302	5.381
Slater DEM	0.226	4.832
Helm DEM	−0.891	5.044
Bamber DEM	0.002	5.248

As shown in Table 5 and Figure 7, the mean elevation differences between the ICESat-2 DEM of the Filchner–Ronne ice shelf and other DEMs are all within 2 m. Meanwhile, mean difference between ICESat-2 DEM and Tandem-X PolarDEM is 1.738 m, which is the largest. The standard deviations are all within 5 m. Similar to the result of the comparison in RIS, elevation differences between FRIS DEM and the five DEMs are mainly distributed in the edge region of ice shelf and cracks in ice shelf. Overall, the results (Table 6 and Figure 8) of the comparison between ICESat-2 AIS DEM with other DEMs bolster show that the DEM elevation uncertainty in the ice shelf edge and internal area with crack is greater than that in flat terrain. In particular, the ICESat-2 DEM shows a generally higher surface height than the TanDEM PolarDEM, which is assumed to be caused by the penetration depth of the X-band (TerraSAR-X and TanDEM-X) into the snowpack. In addition, the standard deviation between the ICESat-2 DEM and the Slater DEM is the smallest, which we believe is due to the fact that the Slater DEM uses 6 years of radar altimetry data and considers the effects of time variation and backscatter.

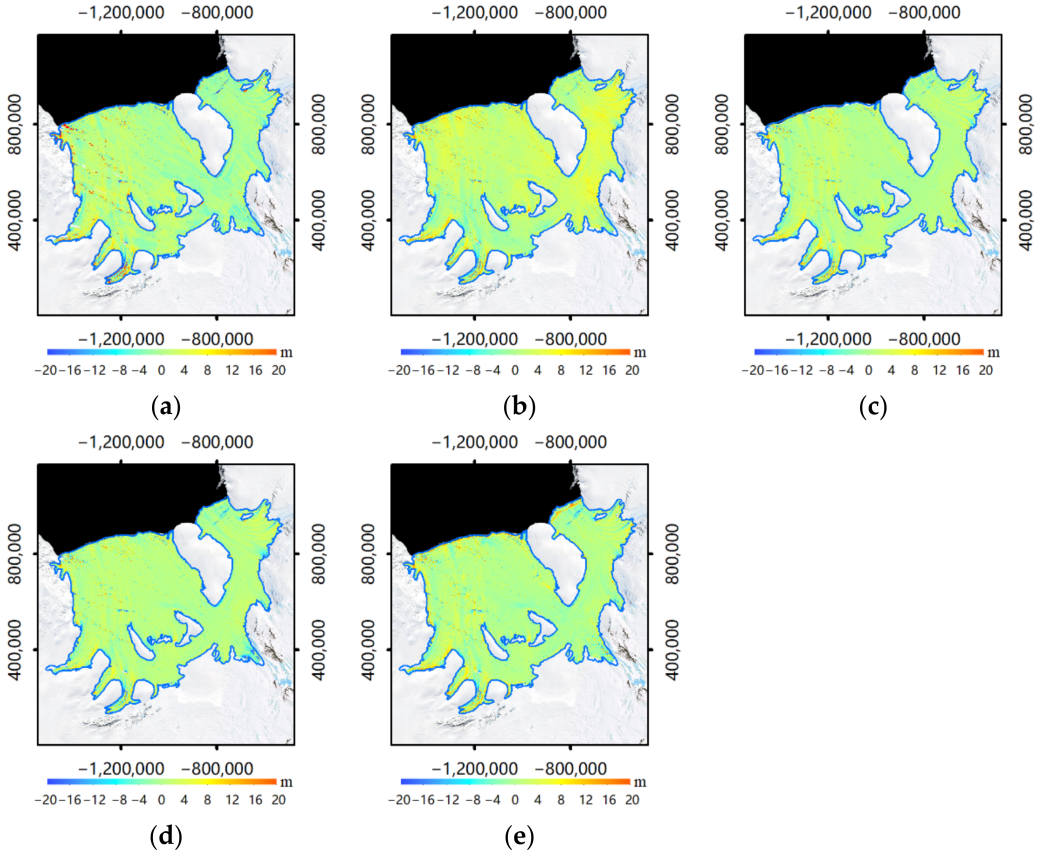


Figure 7. Distribution of elevation differences between the ICESat-2 FRIS DEM and five previously published Antarctic DEMs, i.e., REMA (**a**), TanDEM PolarDEM (**b**), Slater CryoSat-2 DEM (**c**), Helm CryoSat-2 DEM (**d**), Bamber DEM (**e**). Maps are in the polar stereographic projection in meters.

6.2. Comparison with OIB Airborne Lidar Altimetry Data

To evaluate the absolute accuracy of ICESat-2 DEM, 164 862 OIB measurement points that cover RIS and FRIS are used, while OIB data are unavailable in AIS. The bilinear interpolation method was used to obtain the DEM elevation at the exact plane coordinates measured by the airborne laser altimeter and compared with the OIB dataset. Subsequently, the mean difference and standard deviation are calculated. Comparison result shows good agreements between the DEMs and OIB data. Moreover, the mean difference and standard deviation between the airborne data and RIS DEM are −0.016 and 0.918 m, respectively. The DEMs of the Filchner–Ronne ice shelf are −0.533 and 0.718 m.

Figure 9 shows the distribution of difference between RIS DEM and FRIS DEM and OIB airborne data. The results indicate that a larger elevation difference trend appears at the edge of the ice shelf and around the ice cracks. This result is similar to the comparison between ICESat-2 DEM with five other previously published DEMs.

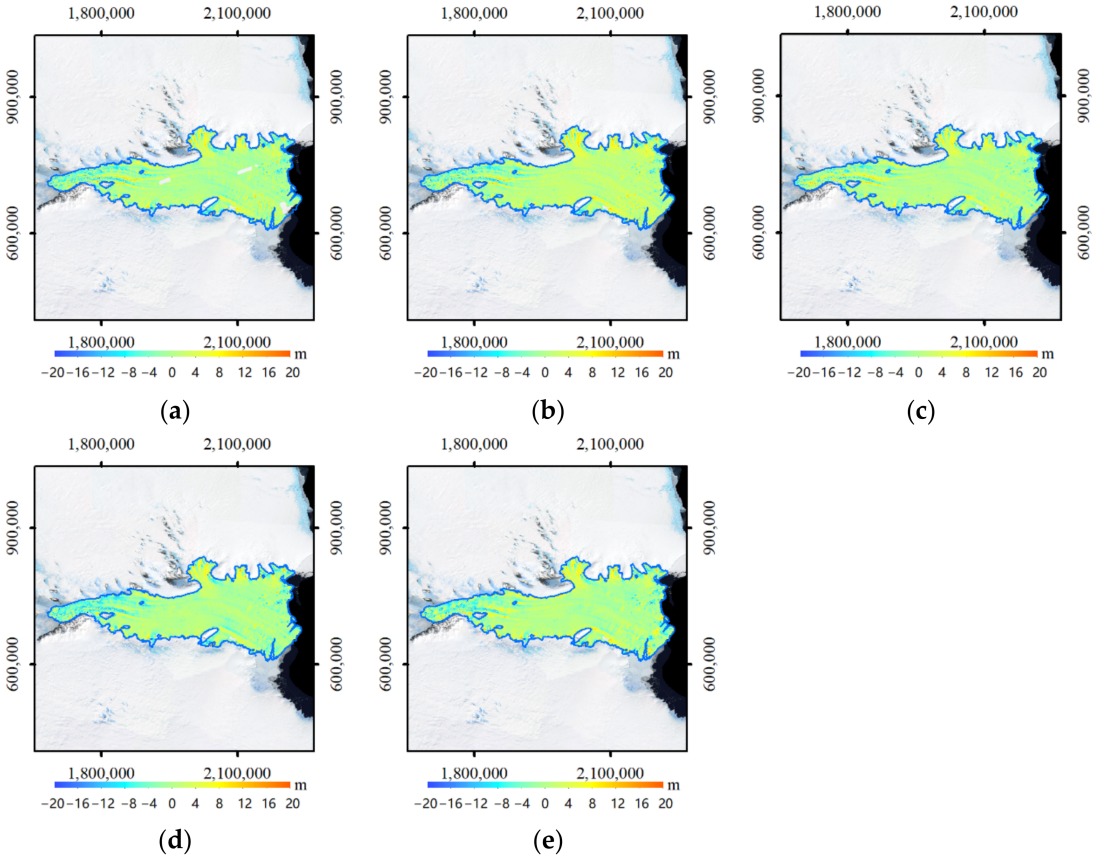


Figure 8. Distribution of elevation differences between the ICESat-2 AIS DEM and five previously published Antarctic DEMs, i.e., REMA (**a**), TanDEM PolarDEM (**b**), Slater CryoSat-2 DEM (**c**), Helm CryoSat-2 DEM (**d**), Bamber DEM (**e**). Maps are in the polar stereographic projection in meters.

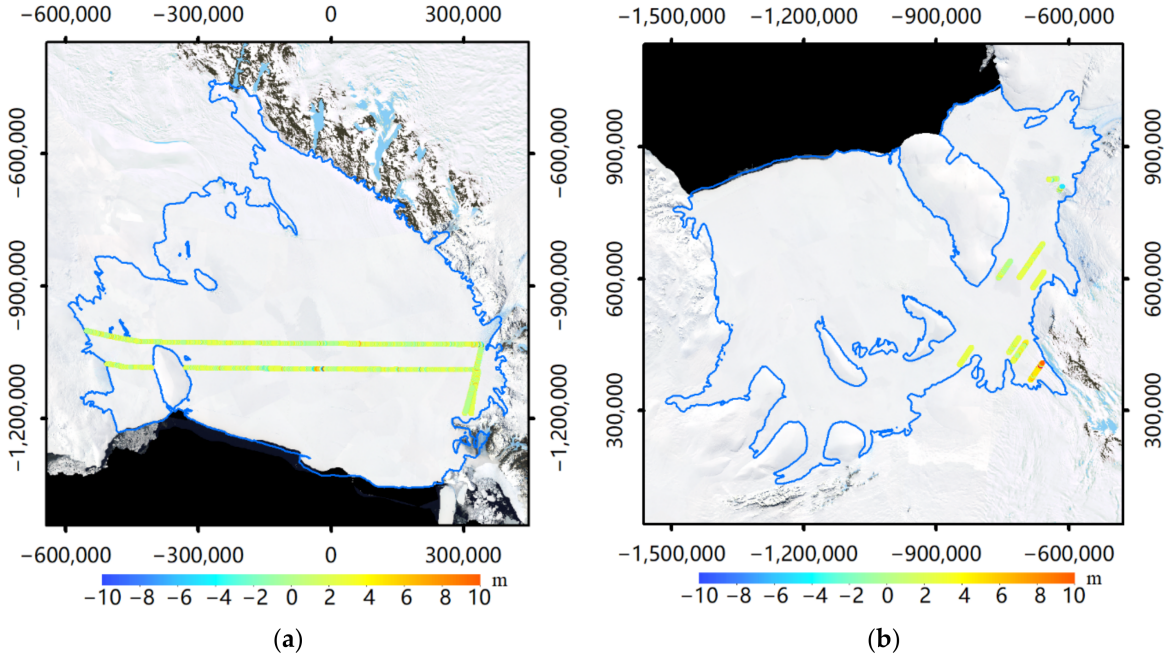


Figure 9. The distribution map of difference between ICESat-2 RIS DEM (**a**) as well as FRIS DEM (**b**) and Operation IceBridge (OIB) elevations. Maps are in the polar stereographic projection in meters.

For a quantitative comparison between the ICESat-2 ice shelf DEM and other Antarctic DEMs, OIB airborne data are used to evaluate individual DEMs, and here the same bilinear interpolation algorithm as in the previous section (Section 6.1) is applied. The comparison result listed in Tables 7 and 8 shows that the ICESat-2 DEM has a better performance than other DEMs.

Table 7. Comparison between the six DEMs and OIB elevations in RIS.

OIB Elevations vs.	Mean/m	Std/m
ICESat-2 RIS DEM	−0.016	0.918
TanDEM-X PolarDEM	5.254	2.203
REMA	0.828	1.805
Slater DEM	0.485	1.853
Helm DEM	0.804	1.733
Bamber DEM	0.187	1.934

Table 8. Comparison between the six DEMs and OIB elevations in FRIS.

OIB Elevations vs.	Mean/m	Std/m
ICESat-2 FRIS DEM	−0.533	0.718
TanDEM-X PolarDEM	1.727	1.924
REMA	0.572	1.096
Slater DEM	−0.097	0.947
Helm DEM	0.077	1.173
Bamber DEM	−0.557	1.382

Although the terrain on the ice shelf is relatively smooth, the slope is still an important factor affecting the accuracy of the DEM. The mean difference and standard deviation in the surface slope for six RIS DEMs between OIB data shown in Figures 10 and 11 illustrate that all their elevation biases become more uncertain with slope increasing within 0.55°, while no significant trend is observed in the standard deviation when the slope is greater than 0.55°. As shown in Figure 12, this result is due to the fact that the RIS is relatively gentle and the number of validation points when the slope is greater than 0.55° is very small. As a result, DEM random errors first increase and then decrease. In the range where the slope is less than 0.55°, the uncertainty of five other RIS DEMs rises faster than that of ICESat-2 RIS DEM (black line in Figure 11). Specifically, the uncertainty of Helm DEM (red line in Figure 11) rises fastest with slope increasing, and the standard deviation is from 1.403 m to 5.902 m. The uncertainty of ICESat-2 RIS DEM rises slowest, and the standard deviation is from 1.215 m to 2.317 m. Values of mean difference and standard deviation between six RIS DEMs and OIB airborne elevation measurements for surface slopes are shown in Table S1.

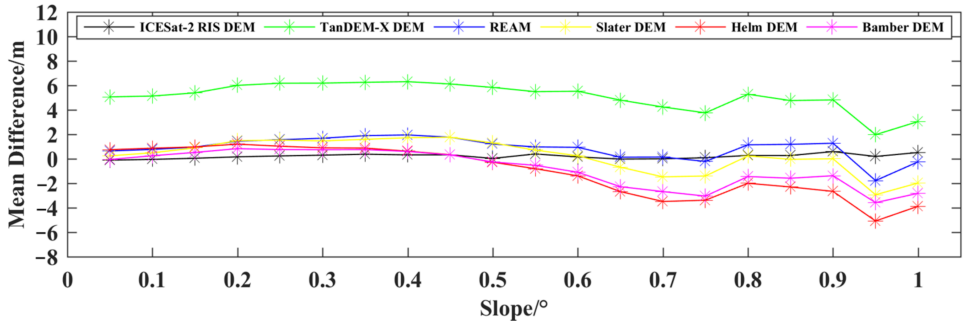


Figure 10. Mean difference between ICESat-2 RIS DEM as well as the five Antarctic DEMs and OIB elevations. The horizontal coordinate is the slope of the surface from 0° to 1° with an interval of 0.05°.

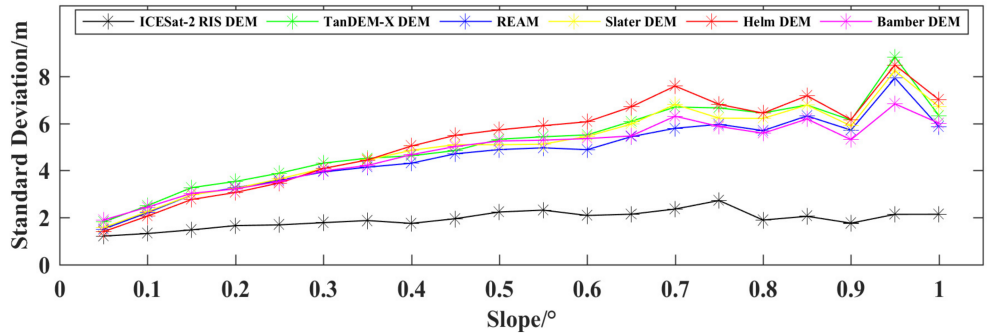


Figure 11. Standard deviations between ICESat-2 RIS DEM as well as the five Antarctic DEMs and OIB elevations. The horizontal coordinate is the slope of the surface from 0° to 1° with an interval of 0.05°.

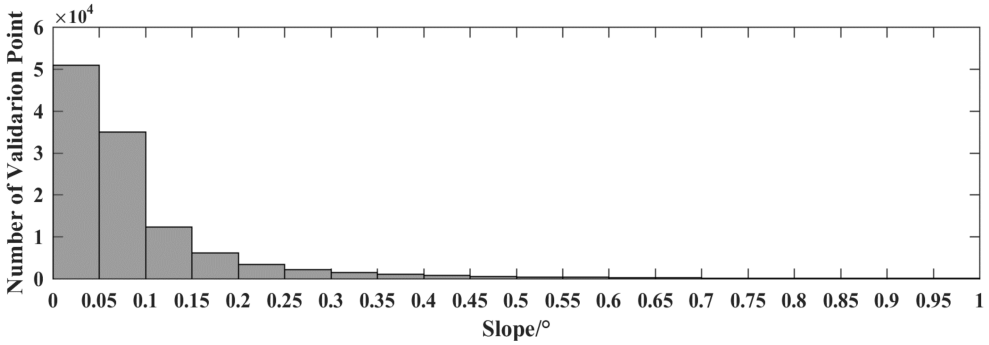


Figure 12. Number of OIB airborne points used to ICESat-2 RIS DEM evaluation. The horizontal coordinate is the slope of the surface from 0° to 1° with an interval of 0.05°.

The mean difference and standard deviation in the surface slope for six FRIS DEMs between OIB data are shown in Figures 13 and 14, respectively. In the same way, we find that elevation biases of ICESat-2 FRIS DEM, TanDEM-X PolarDEM, REMA, and Slater DEM become more uncertain with slope increasing within 0.45°. Meanwhile, no significant trend is observed in the standard deviation when the slope is greater than 0.45°. As with RIS DEM, the number of validation points when the slope is greater than 0.45° in FRIS is very small (Figure 15). However, uncertainty values of Helm DEM and Bamber DEM show no trend with slope change. Compared with the uncertainty values of other DEMs, the uncertainty of ICESat-2 FRIS DEM rises slowest, and the standard deviation is from 0.635 m to 3.59 m in the range of slope less than 0.45°. Values of mean difference and standard deviation between six FRIS DEMs and OIB airborne elevation measurements for the surface slope are shown in Table S2.

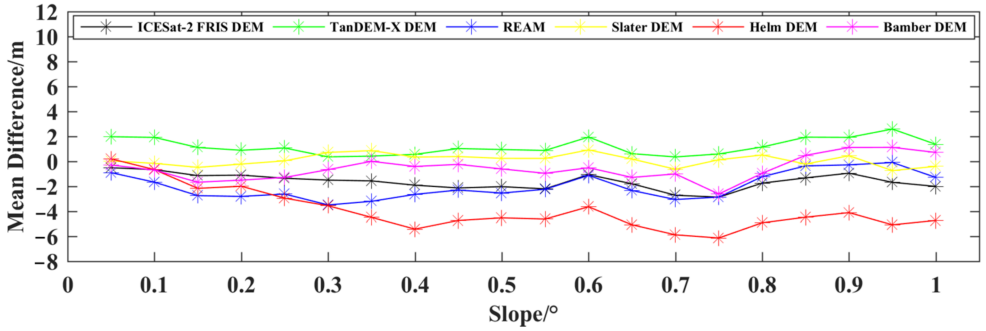


Figure 13. Mean differences between ICESat-2 FRIS DEM as well as the five Antarctic DEMs and OIB elevations. The horizontal coordinate is the slope of the surface from 0° to 1° with an interval of 0.05°.

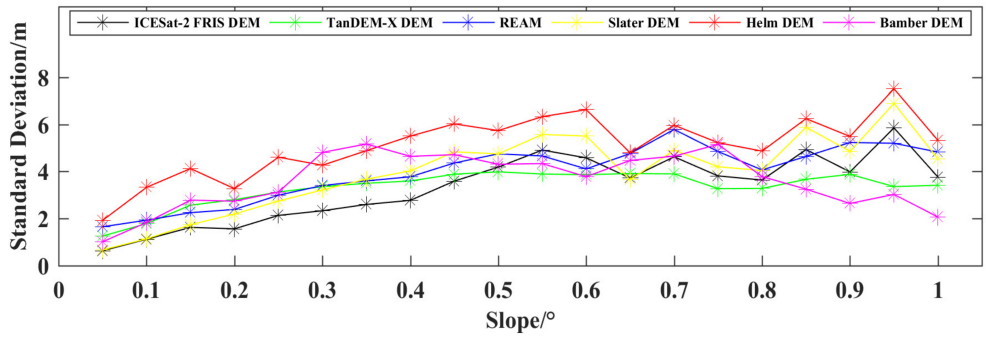


Figure 14. Standard deviations between ICESat-2 FRIS DEM as well as the five Antarctic DEMs and OIB elevations. The horizontal coordinate is the slope of the surface from 0° to 1° with an interval of 0.05°.

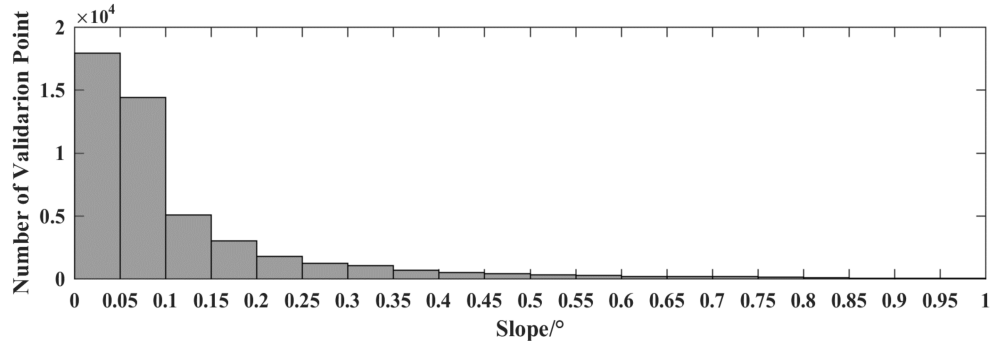


Figure 15. Number of OIB airborne points used to ICESat-2 FRIS DEM evaluation. The horizontal coordinate is the slope of the surface from 0° to 1° with an interval of 0.05°.

7. Conclusions

Based on ICESat-2 LiDAR altimetry data (spanning October 2018 to October 2019), we established RIS, FRIS, and AIS DEMs. These DEMs are established in spatial resolution of 100 m by ordinary kriging interpolation. To choose the optimal variogram of ordinary kriging for ice shelf DEMs, experimental areas are selected in each of RIS, FRIS, and AIF, and the linear and spherical models in kriging interpolation are compared and analyzed. Thus, the spherical model of the variogram of ordinary kriging is used in DEM processing.

The results of a comparison with REMA, TanDEM-X PolarDEM, Slater DEM, Helm DEM, and Bamber DEM show that the new DEMs have the smallest elevation difference with Slater DEM and the largest elevation difference with TanDEM-X PolarDEM. The accuracy of the ICESat-2 DEMs are evaluated by comparing it with OIB ATM data. Validation

results were obtained by bilinear interpolation algorithm: between the FRIS DEM and OIB ATM data, the mean difference was −0.016 m and the standard deviation was 0.918 m; between the FRIS DEM and OIB ATM data, the mean difference was −0.533 and the standard deviation was 0.718 m. The lower elevation accuracy of DEM exists in areas of the edge region of ice shelf and cracks in ice shelf inside, where the terrain is complex. Through comparisons with five previously published Antarctic DEMs, we found that the new ICESat-2 DEM has a better performance than other Antarctic DEMs.

Supplementary Materials: The following are available online at https://www.mdpi.com/article/10.3390/rs13245137/s1. Table S1: Values of mean difference and standard deviation between six RIS DEMs and OIB airborne elevation measurements for surface slope, Table S2: Values of mean difference and standard deviation between six FRIS DEMs and OIB airborne elevation measurements for surface slope.

Author Contributions: Study idea and experimental program design, S.Z. and F.X.; data processing and management, T.G., S.Z., Y.X., J.L., X.L. and F.L.; preparation of original draft, T.G., S.Z. and F.X.; paper review and editing, S.Z. and F.X. All authors have read and agreed to the published version of the manuscript.

Funding: This research was funded by the Nature Natural Science Foundation of China, grant number 41730102; the National Key Research and Development Program of China, grant number 2017YFA0603104; the Fundamental Research Funds for the Central Universities.

Institutional Review Board Statement: Not applicable.

Informed Consent Statement: Not applicable.

Data Availability Statement: Data can be obtained from the author through a reasonable request.

Acknowledgments: We sincerely thank the National Aeronautics and Space Administration for the provision of the ICESat-2 data, the National Snow and Ice Data Center for the provision of IceBridge airborne altimetry data, and the British Antarctic Survey for providing Antarctic coastline products, the United States Geological Survey for LIMA. We also thank the authors of the five digital elevation models used in this paper, all of which are freely obtainable online.

Conflicts of Interest: The authors declare no conflict of interest.

References

1. Rignot, E.; Jacobs, S.; Mouginot, J.; Scheuchl, B. Ice-shelf melting around Antarctica. *Science* **2013**, *341*, 266–270. [CrossRef] [PubMed]
2. Fox, A.J.; Paul, A.; Cooper, R. Measured properties of the Antarctic ice sheet derived from the SCAR Antarctic digital database. *Polar Rec.* **1994**, *30*, 201–206. [CrossRef]
3. Depoorter, M.A.; Bamber, J.L.; Griggs, J.A.; Lenaerts, J.T.M.; Ligtenberg, S.R.M.; van den Broeke, M.R.; Moholdt, G. Calving fluxes and basal melt rates of Antarctic ice shelves. *Nature* **2013**, *502*, 89–92. [CrossRef]
4. Qi, M.; Liu, Y.; Lin, Y.; Hui, F.; Li, T.; Cheng, X. Efficient Location and Extraction of the Iceberg Calved Areas of the Antarctic Ice Shelves. *Remote Sens.* **2020**, *12*, 2658. [CrossRef]
5. Wuite, J.; Nagler, T.; Gourmelen, N.; Escorihuela, M.J.; Hogg, A.E.; Drinkwater, M.R. Sub-Annual Calving Front Migration, Area Change and Calving Rates from Swath Mode CryoSat-2 Altimetry, on Filchner-Ronne Ice Shelf, Antarctica. *Remote Sens.* **2019**, *11*, 2761. [CrossRef]
6. Rignot, E.; Casassa, G.; Gogineni, P.; Krabill, W.; Rivera, A.; Thomas, R. Accelerated ice discharge from the Antarctic Peninsula following the collapse of Larsen B ice shelf. *Geophys. Res. Lett.* **2004**, *31*, L18401. [CrossRef]
7. Stephenson, S.N.; Bindschadler, R.A. Observed velocity fluctuations on a major Antarctic ice stream. *Nature* **1988**, *6184*, 695–697. [CrossRef]
8. Vaughan, D.G.; Arthern, R. CLIMATE CHANGE: Why Is It Hard to Predict the Future of Ice Sheets? *Science* **2007**, *315*, 1503–1504. [CrossRef] [PubMed]
9. Bamber, J.L.; Gomez-Dans, J.L.; Griggs, J.A. A new 1km digital elevation model of the Antarctic derived from combined satellite radar and laser data—Part 1: Data and methods. *Cryosphere* **2009**, *1*, 101–111. [CrossRef]
10. Bamber, J.L.; Griggs, J.A.; Hurkmans, R.T.W.L.; Dowdeswell, J.A.; Gogineni, S.P.; Howat, I.; Mouginot, J.; Paden, J.; Palmer, S.; Rignot, E.; et al. A new bed elevation dataset for Greenland. *Cryosphere* **2013**, *7*, 499–510. [CrossRef]
11. Griggs, J.A.; Bamber, J.L. A new 1km digital elevation model of Antarctica derived from combined radar and laser data—Part 2: Validation and error estimates. *Cryosphere* **2009**, *1*, 113–123. [CrossRef]

12. Wright, A.P.; Siegert, M.J.; Le Brocq, A.M.; Gore, D.B. High sensitivity of subglacial hydrological pathways in Antarctica to small ice-sheet changes. *Geophys. Res. Lett.* **2008**, *35*, L17504. [CrossRef]
13. Wang, Z.; Song, X.; Zhang, B.; Liu, T.; Geng, H. Basal Channel Extraction and Variation Analysis of Nioghalvfjerdsfjorden Ice Shelf in Greenland. *Remote Sens.* **2020**, *12*, 1474. [CrossRef]
14. Xing, Z.; Chi, Z.; Yang, Y.; Chen, S.; Huang, H.; Cheng, X.; Hui, F. Accuracy Evaluation of Four Greenland Digital Elevation Models (DEMs) and Assessment of River Network Extraction. *Remote Sens.* **2020**, *12*, 3429. [CrossRef]
15. Horgan, H.J.; Anandakrishnan, S. Static grounding lines and dynamic ice streams: Evidence from the Siple Coast, West Antarctica. *Geophys. Res. Lett.* **2006**, *33*, L18502. [CrossRef]
16. Paolo, F.S.; Fricker, H.A.; Padman, L. 2015 Volume loss from Antarctic ice shelves is accelerating. *Science* **2015**, *6232*, 327–331. [CrossRef] [PubMed]
17. Smith, B.; Fricker, H.A.; Gardner, A.S.; Medley, B.; Nilsson, J.; Paolo, F.S.; Holschuh, N.; Adusumilli, S.; Brunt, K.; Csatho, B.; et al. Pervasive ice sheet mass loss reflects competing ocean and atmosphere processes. *Science* **2020**, *368*, 1239–1242. [CrossRef] [PubMed]
18. Sutterley, T.C.; Velicogna, I.; Rignot, E.; Mouginot, J.; Flament, T.; van den Broeke, M.R.; van Wessem, J.M.; Reijmer, C.H. Mass loss of the Amundsen Sea Embayment of West Antarctica from four independent techniques. *Geophys. Res. Lett.* **2015**, *41*, 8421–8428. [CrossRef]
19. Young, D.A.; Wright, A.P.; Roberts, J.L.; Warner, R.C.; Young, N.W.; Greenbaum, J.S.; Schroeder, D.M.; Holt, J.W.; Sugden, D.E.; Blankenship, D.D.; et al. A dynamic early East Antarctic Ice Sheet suggested by ice-covered fjord landscapes. *Nature* **2011**, *474*, 72–75. [CrossRef]
20. Yan, S.; Liu, G.; Wang, Y.; Ruan, Z. Accurate Determination of Glacier Surface Velocity Fields with a DEM-Assisted Pixel-Tracking Technique from SAR Imagery. *Remote Sens.* **2015**, *7*, 10898–10916. [CrossRef]
21. Riel, B.; Minchew, B.; Joughin, I. Observing traveling waves in glaciers with remote sensing: New flexible time series methods and application to Sermeq Kujalleq, Greenland. *Cryosphere* **2021**, *15*, 407–429. [CrossRef]
22. Kim, S.; Kim, D. Combined usage of TanDEM-X and CryoSat-2 for generating a high resolution Digital Elevation Model of fast moving ice stream and its application in grounding line estimation. *Remote Sens.* **2017**, *9*, 176. [CrossRef]
23. Bamber, J.L.; Bindschadler, R.A. An improved elevation data set for climate and ice-sheet modeling: Validation with satellite imagery. *Ann. Glaciol.* **1997**, *25*, 430–444. [CrossRef]
24. Helm, V.; Humbert, A.; Miller, H. Elevation and elevation change of Greenland and Antarctica derived from CryoSat-2. *Cryosphere* **2014**, *8*, 1539–1559. [CrossRef]
25. Li, F.; Xiao, F.; Zhang, S.K.; E, D.C.; Cheng, X.; Hao, W.F.; Yuan, L.X.; Zuo, Y.W. DEM development and precision analysis for Antarctic ice sheet using CryoSat-2 altimetry data. *Chin. J. Geophys.* **2017**, *5*, 1617–1629.
26. Slater, T.; Shepherd, A.; McMillan, M.; Muir, A.; Gilbert, L.; Hogg, A.E.; Konrad, H.; Parrinello, T. A new digital elevation model of Antarctica derived from CryoSat-2 altimetry. *Cryosphere* **2018**, *12*, 1551–1562. [CrossRef]
27. DiMarzio, J.; Brenner, A.; Schutz, R.C.; Shuman, A.; Zwally, H.J. *GLAS/ICESat 500 m Laser Altimetry Digital Elevation Model of Antarctica*; Version 1; NASA National Snow and Ice Data Center Distributed Active Archive Center: Boulder, CO, USA, 2007.
28. Rizzoli, P.; Martone, M.; Gonzalez, C.; Wecklich, C.; Borla Tridon, D.; Bräutigam, B.; Bachmann, M.; Schulze, D.; Fritz, T.; Huber, M.; et al. Generation and performance assessment of the global TanDEM-X digital elevation model. *ISPRS J. Photogramm.* **2017**, *132*, 119–139. [CrossRef]
29. Abdullahi, S.; Wessel, B.; Huber, M.; Wendleder, A.; Roth, A.; Kuenzer, C. Estimating Penetration-Related X-Band InSAR Elevation Bias: A Study over the Greenland Ice Sheet. *Remote Sens.* **2019**, *11*, 2903. [CrossRef]
30. Gardelle, J.; Berthier, E.; Arnaud, Y. Impact of resolution and radar penetration on glacier elevation changes computed from DEM differencing. *J. Glaciol.* **2012**, *58*, 419–422. [CrossRef]
31. Gourmelen, N.; Escorihuela, M.J.; Shepherd, A.; Foresta, L.; Muir, A.; Garcia-Mondéjar, A.; Roca, M.; Baker, S.G.; Drinkwater, M.R. CryoSat-2 swath interferometric altimetry for mapping ice elevation and elevation change. *Adv. Space Res.* **2018**, *62*, 1226–1242. [CrossRef]
32. Wessel, B.; Huber, M.; Wohlfart, C.; Marschalk, U.; Kosmann, D.; Roth, A. Accuracy assessment of the global TanDEM-X Digital Elevation Model with GPS data. *ISPRS J. Photogramm.* **2018**, *139*, 171–182. [CrossRef]
33. Du, Y.N.; Feng, G.C.; Li, Z.W.; Zhu, J.J. Generation of high precision DEM from TerraSAR-X/TanDEM-X. *Chin. J. Geophys.* **2015**, *9*, 3089–3102.
34. Gruber, A.; Wessel, B.; Martone, M.; Roth, A. The TanDEM-X DEM Mosaicking: Fusion of Multiple Acquisitions Using InSAR Quality Parameters. *IEEE J. Sel. Top. Appl. Earth Obs. Remote Sens.* **2016**, *9*, 1047–1057. [CrossRef]
35. Howat, I.M.; Porter, C.; Smith, B.E.; Noh, M.; Morin, P. The Reference Elevation Model of Antarctica. *Cryosphere* **2019**, *13*, 665–674. [CrossRef]
36. Rao, Y.S.; Rao, K.S. Comparison of DEMs derived from INSAR and optical stereo techniques. In Proceedings of the Third ESA International Workshop on ERS SAR Interferometry, Frascati, Italy, 1–5 December 2003; Available online: http://citeseerx.ist.psu.edu/viewdoc/download?doi=10.1.1.212.4788&rep=rep1&type=pdf (accessed on 5 October 2020).
37. Markus, T.; Neumann, T.; Martino, A.; Abdalati, W.; Brunt, K.; Csatho, B.; Farrell, S.; Fricker, H.; Gardner, A.; Harding, D.; et al. The Ice, Cloud, and land Elevation Satellite-2 (ICESat-2): Science requirements, concept, and implementation. *Remote Sens. Environ.* **2017**, *190*, 260–273. [CrossRef]

38. Abdalati, W.; Zwally, H.J.; Bindschadler, R.; Csatho, B.; Farrell, S.L.; Fricker, H.A.; Harding, D.; Kwok, R.; Lefsky, M.; Markus, T.; et al. The ICESat-2 Laser Altimetry Mission. *Proc. IEEE* **2010**, *98*, 735–751. [CrossRef]
39. Shen, X.Y.; Ke, C.Q.; Yu, X.N.; Cai, Y.; Fan, Y.B. Evaluation of Ice, Cloud, And Land Elevation Satellite-2 (ICESat-2) land ice surface heights using Airborne Topographic Mapper (ATM) data in Antarctica. *Int. J. Remote Sens.* **2021**, *42*, 2556–2573. [CrossRef]
40. Fricker, H.A.; Hyland, G.; Coleman, R.; Young, N.W. Digital elevation models for the Lambert Glacier–Amery Ice Shelf system, East Antarctica, from ERS-1 satellite radar altimetry. *J. Glaciol.* **2000**, *46*, 553–560. [CrossRef]
41. Griggs, J.A.; Bamber, J.L. Antarctic ice-shelf thickness from satellite radar altimetry. *J. Glaciol.* **2011**, *57*, 485–498. [CrossRef]
42. Nguyen, A.T.; Herring, T.A. Analysis of ICESat data using Kalman filter and kriging to study height changes in East Antarctica. *Geophys. Res. Lett.* **2005**, *32*, L23S03. [CrossRef]
43. Strößenreuther, U.; Horwath, M.; Schröder, L. How Different Analysis and Interpolation Methods Affect the Accuracy of Ice Surface Elevation Changes Inferred from Satellite Altimetry. *Math. Geosci.* **2020**, *52*, 499–525. [CrossRef]
44. Chen, C.; Li, Y.A. Fast Global Interpolation Method for Digital Terrain Model Generation from Large LiDAR-Derived Data. *Remote Sens.* **2019**, *11*, 1324. [CrossRef]
45. Koo, Y.; Xie, H.; Kurtz, N.T.; Ackley, S.F.; Mestas-Nuñez, A.M. Weekly Mapping of Sea Ice Freeboard in the Ross Sea from ICESat-2. *Remote Sens.* **2021**, *13*, 3277. [CrossRef]
46. Li, Y.Z.; McGillicuddy, D.J.; Dinniman, M.S.; Klinck, J.M. Processes influencing formation of low-salinity high-biomass lenses near the edge of the Ross Ice Shelf. *J. Mar. Syst.* **2017**, *166*, 108–119. [CrossRef]
47. Grosfeld, K.; Schröder, M.; Fahrbach, E.; Gerdes, R.; Mackensen, A. How iceberg calving and grounding change the circulation and hydrography in the Filchner Ice Shelf-Ocean System. *J. Geophys. Res. Ocean.* **2001**, *106*, 9039–9055. [CrossRef]
48. Yu, J.; Liu, H.X.; Jezek, K.C.; Warner, R.C.; Wen, J. Analysis of velocity field, mass balance, and basal melt of the Lambert Glacier–Amery Ice Shelf system by incorporating Radarsat SAR interferometry and ICESat laser altimetry measurements. *J. Geophys. Res.* **2010**, *115*, B11102. [CrossRef]
49. Robert, B.; Patricia, V.; Andrew, F.; Adrian, F.; Jerry, M.; Douglas, B.; Sara, J.P.; Brian, G.; David, G. The Landsat Image Mosaic of Antarctica. *Remote Sens. Environ.* **2008**, *112*, 4214–4426.
50. Smith, B.; Fricker, H.A.; Holschuh, N.; Gardnerd, A.S.; Adusumillib, S.; Brunte, K.M.; Csathog, B.; Harbecke, K.; Hutha, A.; Neumanne, T.; et al. Land ice height-retrieval algorithm for NASA's ICESat-2 photon-counting laser altimeter. *Remote Sens. Environ.* **2019**, *233*, 111352. [CrossRef]
51. Neumann, T.A.; Martino, A.J.; Markus, T.; Bae, S.; Bock, M.R.; Brenner, A.C.; Brunt, K.M.; Cavanaugh, J.; Fernandes, S.T.; Hancock, D.W.; et al. The Ice, Cloud, and Land Elevation Satellite—2 mission: A global geolocated photon product derived from the Advanced Topographic Laser Altimeter System. *Remote Sens. Environ.* **2019**, *233*, 111325. [CrossRef] [PubMed]
52. Brunt, K.M.; Neumann, T.A.; Smith, B.E. Assessment of ICESat-2 Ice Sheet Surface Heights, Based on Comparisons over the Interior of the Antarctic Ice Sheet. *Geophys. Res. Lett.* **2019**, *46*, 13072–13078. [CrossRef]
53. Li, R.X.; Li, H.W.; Hao, T.; Qiao, G.; Cui, H.T.; He, Y.Q.; Hai, G.; Xie, H.; Cheng, Y.; Li, B.F. Assessment of ICESat-2 ice surface elevations over the Chinese Antarctic Research Expedition (CHINARE) route, East Antarctica, based on coordinated multi-sensor observations. *Cryosphere* **2021**, *15*, 3083–3099. [CrossRef]
54. Kurtz, N.T.; Farrell, S.L.; Studinger, M.; Galin, N.; Harbeck, J.P.; Lindsay, R.; Onana, V.D.; Panzer, B.; Sonntag, J.G. Sea ice thickness, freeboard, and snow depth products from Operation IceBridge airborne data. *Cryosphere* **2013**, *7*, 1035–1056. [CrossRef]
55. Martin, C.F.; Krabill, W.B.; Manizade, S.S.; Russell, R.L.; Sonntag, J.G.; Swift, R.N.; Yungel, J.K. *Airborne Topographic Mapper Calibration Procedures and Accuracy Assessment*; NASA: Washington, DC, USA, 2012.
56. Studinger, M. *IceBridge ATM L2 Icessn Elevation, Slope, and Roughness*; Version 2; NASA National Snow and Ice Data Center Distributed Active Archive Center: Boulder, CO, USA, 2014.
57. Cook, A.J.; Murray, T.; Luckman, A.; Vaughan, D.G.; Barrand, N.E. A new 100-m Digital Elevation Model of the Antarctic Peninsula derived from ASTER Global DEM: Methods and accuracy assessment. *Earth Syst. Sci. Data* **2012**, *4*, 129–142. [CrossRef]
58. Oliver, M.A.; Webster, R. Kriging: A method of interpolation for geographical information systems. *Int. J. Geogr. Inf. Syst.* **1990**, *4*, 313–332. [CrossRef]
59. Oliver, M.A.; Webster, R. *Basic Steps in Geostatistics: The Variogram and Kriging*; Springer International Press: Cham, Switzerland, 2015; p. 112.
60. Bamber, J.; Gomez-Dans, J.L. The accuracy of digital elevation models of the Antarctic continent. *Earth Planet. Sci. Lett.* **2005**, *237*, 516–523. [CrossRef]
61. Ray, R.D. *A Global Ocean Tide Model from TOPEX/POSEIDON Altimetry: GOT99. 2. NASA Technical Memorandum 209478*; Goddard Space Flight Center: Washington, DC, USA, 1999.
62. Neumann, T.A.; Brenner, A.; Hancock, D.; Robbins, J.; Saba, J.; Harbeck, K.; Gibbons, A.; Lee, J.; Luthcke, S.B.; Rebold, T. Algorithm Theoretical Basis Document (ATBD) for Global Geolocated Photons ATL03, Version 3, Release Date 1 April 2020. 2020. Available online: https://nsidc.org/sites/nsidc.org/files/technical-references/ICESat2_ATL03_ATBD_r003.pdf (accessed on 5 October 2020).
63. Gerrish, L.; Fretwell, P.; Cooper, P. *High Resolution Vector Polylines of the Antarctic Coastline*; Version 7.2; UK Polar Data Centre, Natural Environment Research Council and UK Research and Innovation: Cambridge, UK, 2020.